Environmental Science & Technology

Article

Cite This: *Environ. Sci. Technol.* 2019, 53, 7673−7682

pubs.acs.org/est

Probing the Surface Reactivity of Pyrogenic Carbonaceous Material (PCM) through Synthesis of PCM-Like Conjugated Microporous Polymers

Zhao Li,[†] Jingdong Mao,[‡] Wenying Chu,[‡] and Wenqing Xu*,[†]

[†]Department of Civil and Environmental Engineering, Villanova University, Villanova, Pennsylvania 19085, United States
[‡]Department of Chemistry and Biochemistry, Old Dominion University, Norfolk, Virginia 23529, United States

Supporting Information

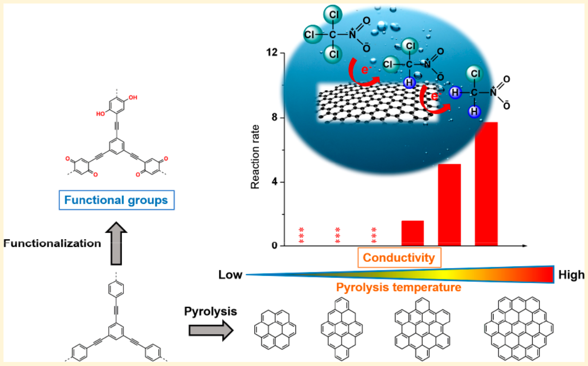

ABSTRACT: Pyrogenic carbonaceous matter (PCM) is redox-active and promotes both abiotic and biotic reactions in the environment, possibly as a result of its conductivity and phenolic/quinone functional groups. However, due to the complexity of PCM, the contribution of conductivity or phenolic/quinone functional groups to its redox activity is poorly understood, which hinders its potential engineering applications. Here, we synthesized tunable conjugated microporous polymers (CMPs) that possess key properties of PCM, which can be used as PCM analogues to provide insights to PCM reactivity. Specifically, controlled incorporation of phenolic moieties into CMPs during polymer synthesis affected electron-donating capacity, while carbonization of CMPs at various temperatures altered conductivity. Both properties were then correlated with PCM reactivity measured by the decay kinetics of a model pollutant trichloronitromethane. We demonstrate that some of the prepared CMPs enabled transformation of trichloronitromethane, while no decay was observed in the absence of CMPs. Results of further investigation suggest that trichloronitromethane decay occurs by reductive dechlorination, suggesting that CMPs are electron donors and the first dissociative electron transfer from CMPs was likely to be the rate-limiting step. Conductivity but not electron-donating capacity was positively correlated with CMP-mediated trichloronitromethane decay kinetics, suggesting an important role of the electron transfer kinetics at the interface for PCM-mediated transformation of environmental pollutants.

INTRODUCTION

Pyrogenic carbonaceous matter (PCM) is the solid residue from the incomplete combustion of fossil fuels or biomass under oxygen-limited conditions,[1] which includes black carbon (fossil fuel soot and biomass char), engineered carbons (biochar and activated carbon), and related materials, such as graphene and nanotubes.[2] PCM has a strong affinity toward pollutants as a result of its porous structure, large surface area, and diverse surface functional groups. As a result, PCM has been traditionally viewed as a passive adsorbent and is widely used as amendments in contaminated soils and sediments to strip pollutants from the aqueous phase.[3−5] Recent studies suggest that PCM is redox-active and can therefore participate in environmental redox processes that are important for the transformation of pollutants and in geochemical cycles of redox-active elements.[6−8] For instance, it has been reported that the abiotic transformation of certain halogenated and nitrogenous compounds by sulfide can be promoted by PCM, while no degradation of these compounds was observed in the absence of PCM.[6,9−12] Furthermore, PCM can shuttle electrons among microbes or between microbes and minerals (e.g., hematite and ferrihydrite), thereby facilitating interspecies electron transfer or the reductive dissolution of minerals in the environment.[13] Therefore, it is important to understand the key properties of PCM that contribute to its observed redox activity.

PCM is amorphous, without long-range molecular order, and contains a range of oxygenated functional groups,[14] including carbonyls, lactones, carboxylic acids, and quinones. Quinones are especially noteworthy for participating in redox reactions.[15] During biomass burning, polyaromatic ring structures (e.g., graphitic regions) are also formed within amorphous PCM, which can facilitate the delocalization of electrons and, thereby, contribute to the electrical conductivity of PCM.[16,17] Previous studies have suggested that both redox-active moieties (e.g., quinone/hydroquinone pairs) and polyaromatic ring structures of PCM contribute to their redox activity.[18−21] Specifically, it was proposed that PCM could act as a conductor and, thereby, facilitate redox reactions

Received: March 23, 2019
Revised: May 28, 2019
Accepted: June 6, 2019
Published: June 6, 2019

DOI: 10.1021/acs.est.9b01772

by the polyaromatic ring structures.[10,19,22] On the other hand, PCM could, in some cases, function as a battery, where electrons can be released and stored through redox-active moieties.[21,23] However, the properties of PCM used in these studies, namely, their surface moieties and polyaromatic ring structures, were often simultaneously altered, because it is difficult to isolate the individual properties.[24,25] Therefore, research efforts to uncover the key properties of PCM responsible for its redox activity are hindered as a result of the lack of a systematic approach, whereby the individual properties of PCM can be systematically varied and investigated. Moreover, using a mediated electrochemical approach, researchers suggested that phenolic moieties were responsible for the associated electron-donating capacity (EDC), while both quinones and polyaromatic ring structures contributed to the electron-accepting capacity (EAC) of PCM.[22] However, EDC and EAC only reflect the pools of electrons that are available for redox reactions and, thus, do not predict the extent of pollutant transformation because these processes are often kinetically limited. Therefore, the relationship among the EDC/EAC of PCM, the electron transfer kinetics at the interface, and the impact on the degradation of contaminants under environmentally relevant conditions require further investigation.

In this study, we aim to provide a platform where individual properties of PCM can be systematically studied. In particular, PCM-like polymers, namely, conjugated microporous polymers (CMPs), were synthesized according to previously established methods.[26−28] Similar to PCM, CMPs are a class of materials that are highly conjugated and amorphous with no long-range molecular order. Moreover, CMPs are similar to PCM in that they are both microporous and have large surface areas as well as high adsorption capacities for organic contaminants. Furthermore, the individual properties of CMPs, specifically their functional groups and conductivity, can be conferred during the synthesis process, whereby particular functional groups are incorporated by selecting appropriate monomers during synthesis.[27,29] Most CMPs, although conjugated in nature, are not electrically conductive as a result of their amorphous nature and the lack of orbital overlap among the twisted benzene rings in CMPs. Therefore, to systematically vary the conductivity of CMPs, we applied a method that has been traditionally used in the field, graphitizing the structure of CMPs through high-temperature carbonization.[10,30] Upon obtaining CMPs, where functional groups and conductivity were individually varied, their redox reactivities were assessed by their ability to facilitate trichloronitromethane (TCNM) decay. For this study, we selected TCNM, a fumigant and disinfection byproduct in water treatment, as a model pollutant. Detailed characterizations of the decay kinetics, pH effect, and transformation products were conducted. A correlation analysis was carried out between the degradation rates of TCNM and measured EDC values and conductivity of CMPs to understand the critical factors that are responsible for the redox activity of PCM.

■ MATERIALS AND METHODS

Chemicals. Detailed information for chemicals is provided in the Supporting Information (Text S1 of the Supporting Information). All chemicals were used without further purification.

Synthesis of CMPs. CMPs were synthesized by Pd(0)/Cu(I)-catalyzed Sonogashira−Hagihara cross-coupling chemistry, by which a 1,4-dibromobenzene node was connected to a rigid 1,3,5-triethynylbenzene strut following the protocol developed and optimized by Cooper's group.[31,32] The synthetic route is shown in eq 1. Briefly, 1,3,5-triethynylbenzene (3.0 mmol), 1,4-dibromobenzene (3.0 mmol), tetrakis(triphenylphosphine)palladium(0) (150 mg), and copper(I) iodide (45 mg) were dissolved in a mixture of toluene (20 mL) and triethylamine (20 mL) for 0.5 h. The mixture was kept in the dark and heated to 80 °C for 72 h under a nitrogen atmosphere. After the reactor was cooled to room temperature, the products were washed with chloroform, followed by water, methanol, and acetone, to remove the unreacted monomers and catalyst residues. The products were then purified by Soxhlet extraction with methanol for 48 h and subsequently dried under a vacuum (0.17 atm) at 100 °C for 24 h. The obtained CMPs were designated as CMP-1 (yield of 106.85%) and appeared as a light brown powder. The CMPs containing phenolic moieties were synthesized following the same route, except that 2,5-dibromohydroquinone was substituted for 1,4-dibromobenzene. The obtained CMPs were designated as CMP-2 (yield of 114.3%) and appeared as a dark brown powder. The yield is calculated by dividing the obtained mass of the product over the expected mass. Specifically, the expected mass of products represents, under ideal conditions, an alkyne on one monomer reacting with a bromophenyl group on another monomer to form the network, releasing hydrogen bromide (HBr) at the same time. However, not all bromophenyl on the monomer will react with alkyne in reality, which has resulted in the higher than 100% yields in some cases.

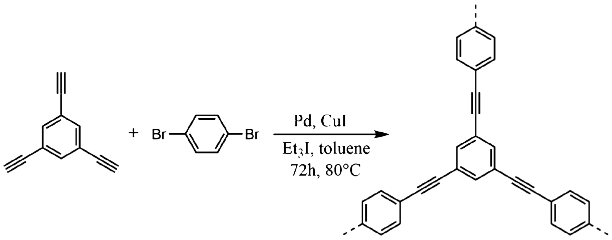

(1)

Carbonized CMPs. To systematically vary the conductivity of the CMPs, previously synthesized CMP-1 was carbonized at different pyrolysis temperatures and products were designated as CMP-1-*X* (where *X* indicates the pyrolysis temperature in degrees Celsius). In brief, 0.9 g of CMP-1 was placed in a model 1600 serial CM tube furnace (CM Furnace, Inc., Bloomfield, NJ, U.S.A.) and pyrolyzed at various temperatures (600, 700, 800, and 900 °C) under a N_2 flow of 50 mL/min. The furnace was ramped up to the desired temperature at a rate of 5 °C/min, then held for 2 h, and subsequently cooled to room temperature. The yields for CMP-1-600, CMP-1-700, CMP-1-800, and CMP-1-900 were 89.5, 86.7, 81.8, and 80.2%, respectively.

Characterization of CMP-1, CMP-2, and the Carbonized CMPs. The surface areas and pore size distributions of CMP-1, CMP-2, CMP-1-600, CMP-1-700, CMP-1-800, and CMP-1-900 were measured by a Brunauer−Emmett−Teller (BET) surface analyzer NOVA 3000e (Quantachrome Instruments, Boynton Beach, FL, U.S.A.) using nitrogen gas at 77.3 K. All samples were outgassed at 110 °C for 18 h prior to measurement. The surface areas were calculated using data

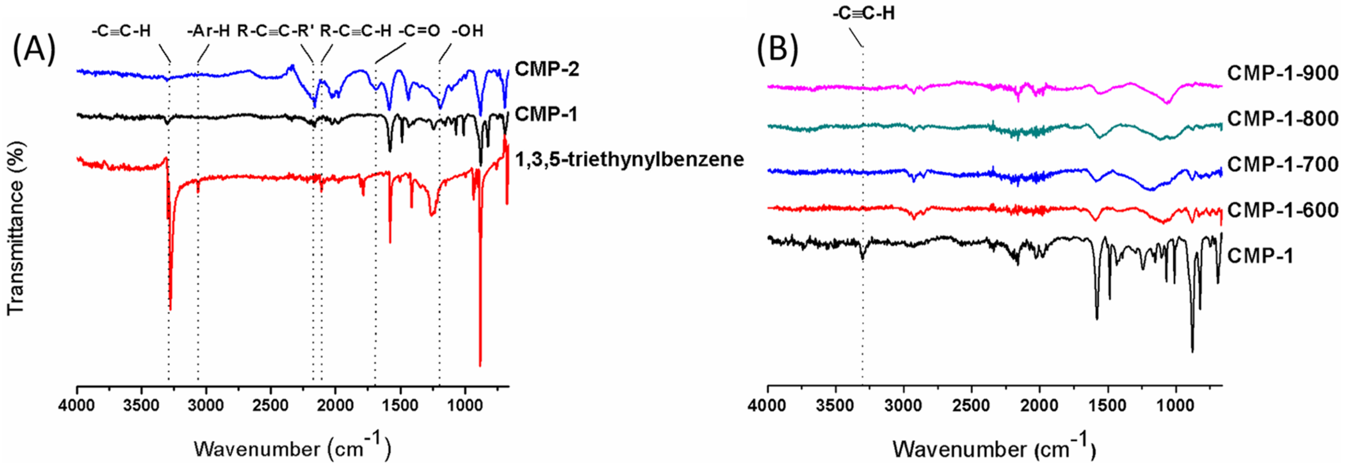

Figure 1. (A) FTIR of 1,3,5-triethynylbenzene, CMP-1, and CMP-2. (B) FTIR of CMP-1, CMP-1-600, CMP-1-700, CMP-1-800, and CMP-1-900.

collected from 0.015 to 0.05 p/p_0. The pore size distributions of the CMPs were derived from the adsorption branch of the isotherm using the non-local density functional theory (NLDFT) model.[33] The infrared spectra of the samples were collected on a PerkinElmer 1600 series FTIR spectrophotometer, where 32 scans were accumulated with a resolution of 4 cm^{-1} in the range of 4000−400 cm^{-1} for each sample. All of the nuclear magnetic resonance (NMR) experiments were performed on a Bruker Avance 400 spectrometer at a ^{13}C frequency of 100 MHz with 4 mm sample rotors in a double-resonance probe head. The ^{13}C multiple cross-polarization/magic angle spinning (multi-CP/MAS) NMR technique was used to provide quantitative structural information for the CMPs.[34] The quantitative spectra were recorded at a spinning speed of 14 kHz, with a 90° ^{13}C pulse length of 4 μs. All of the spectra had good signal-to-noise ratios, with very small (<3%) spinning sidebands and minimal overlapping center bands. Multi-CP experiments combined with 68 μs dipolar dephasing (multi-CP/DD) were also employed to obtain sub-spectra of the non-protonated C and mobile groups. Scanning electron microscopy (SEM, Hitachi S-4800) with an accelerating voltage of 10 kV was used to obtain information on the morphology of the CMPs. The electrical conductivity of the CMPs was measured using a two-probe bed technique as described in our previous publication.[10] Increasing pressure was applied to a packed bed of CMPs by two copper pistons. The electrical resistance between the two copper pistons was recorded using a Keithley 2400 SourceMeter unit (SMU) instrument (Tektronix, Beaverton, OR, U.S.A.), and the length was measured by vernier calipers. Accordingly, the electrical conductivity σ (S m^{-1}) was calculated using the following formula:

$$\sigma = \frac{l - l_0}{(R - R_0)A} \tag{2}$$

where σ is the CMPs electrical conductivity, l and l_0 are the packed-bed and empty-bed lengths, respectively, R and R_0 are the measured electrical resistance in the presence and absence of the CMPs, respectively, and A is the cross-sectional area of the bed. The measured electrical conductivity of the empty bed was constant over an applied pressure between 0 and 4 MPa.

Electron-Donating Capacity (EDC) of CMPs. A potentiometric titration method was adapted to determine the EDC values of CMPs in this study.[35] Briefly, 2.5 g/L CMPs and a blank in 0.2 M ammonium buffer (NH_4Cl and NH_4OH) at pH 10 were titrated in the dark with oxidizing or reducing agents under an argon atmosphere as follows: First, an excess of $NaBH_4$ (0.025 M) was added to the suspension to fully reduce the sample. Subsequently, 0.05 M I_2 was added drop by drop to the suspension to construct an oxidizing titration curve. During the titration, the redox potential [millivolts versus standard hydrogen electrode (SHE)] of the suspension was recorded against the volume of the titrant, which was converted to the electron exchange capacity (EEC) of the sample (moles of electrons per gram of CMPs). We assumed that an eight electron oxidation of $NaBH_4$ and a two electron reduction of I_2 occurred at pH 10. The EEC of the samples can thereby be calculated using the following equation:

$$\text{EEC (mmol of e}^-\text{/g)} = C_i V_i \frac{2e^-}{m_c} \tag{3}$$

where C_i is the concentration of the I_2 solution, V_i is the volume of I_2 solution added to reoxidize the suspension of CMPs, m_c is the mass of CMPs in the suspension, and $2e^-$ is the number of electrons that each mole of I_2 can accept, assuming that I^- is the final product. Finally, the EDC was determined according to the differences in the consumption of I_2 between samples containing CMPs and the blank in 0.2 M ammonium buffer at 535 mV, where I_2 was the dominant species and the EDC of CMPs was completely exhausted.

Batch Reactor Experiments. Kinetic studies on the degradation of TCNM were performed in the presence of the CMPs in the batch reactors. Briefly, 15 μL of TCNM stock solution [1000 mg/L in methyl *tert*-butyl ether (MTBE)] was spiked to 14 mL borosilicate glass reactors containing pre-weighed CMPs to obtain an initial concentration of 6.52 μmol/L. A total of 0.7 g/L CMP-1, CMP-2, CMP-1-600, CMP-1-700, CMP-1-800, and CMP-1-900 were used in this study. To eliminate headspace, all of the reactors were filled up with 10 mM phosphate buffer at pH 7. The vials were capped with Teflon-lined septa and placed on a rotator in the dark at 30 rpm and 25 °C. The samples were periodically collected for chemical analysis. To separate the aqueous and solid phases, the samples were centrifuged at 3500 rpm for 3 min at 0 °C. A temperature of 0 °C was used to minimize any potential degradation of TCNM during the sampling process. Both the aqueous and solid phases were then extracted by shaking with MTBE for 3 min. To quantify TCNM and its transformation

DOI: 10.1021/acs.est.9b01772
Environ. Sci. Technol. 2019, 53, 7673−7682

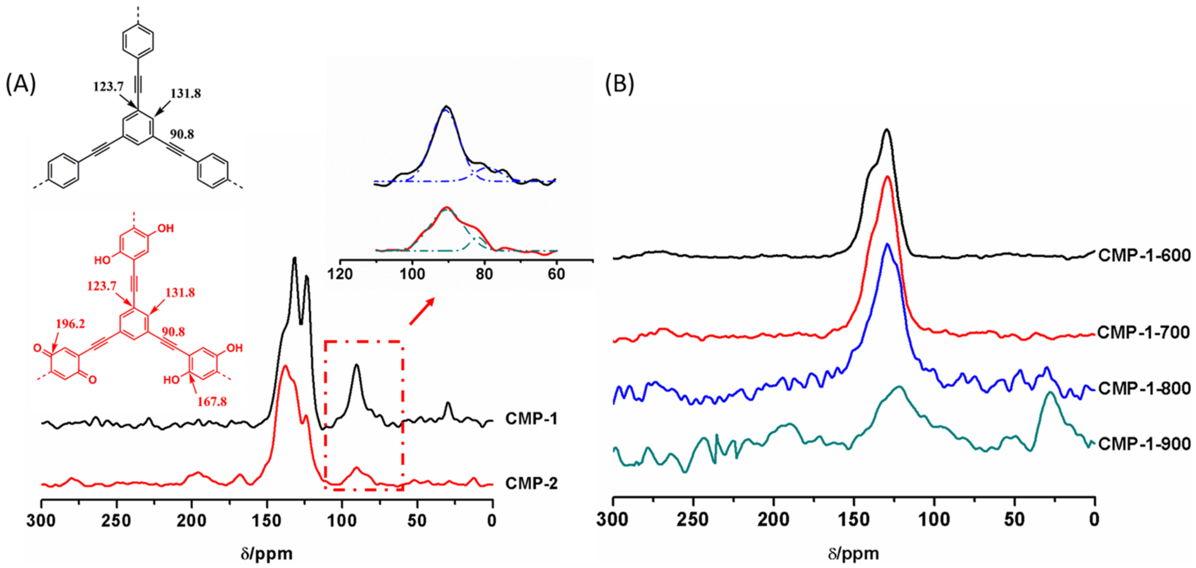

Figure 2. (A) Solid-state ^{13}C multi-CP/MAS NMR spectra of CMP-1 (black) and CMP-2 (red). (B) Solid-state ^{13}C multi-CP/MAS NMR spectra of CMP-1-600, CMP-1-700, CMP-1-800, and CMP-1-900. All spectra were recorded at a spinning speed of 14 kHz with a 90° ^{13}C pulse length of 4 μs. All of the spectra had good signal-to-noise ratios with very small (<3%) spinning sidebands and minimal overlapping center bands.

products, including dichloronitromethane (DCNM) and chloronitromethane (CNM), the extracts were subsequently analyzed by gas chromatography coupled with mass spectroscopy (GC, Agilent 6890N; MS, Agilent 5973 MS, Santa Clara, CA, U.S.A.). Ion chromatography (IC) coupled with a conductivity detector (CDD-10A, Shimazu) was used to quantify the formation of chloride from the TCNM decay.

■ RESULTS AND DISCUSSION

Characterization of the Synthesized PCM-Like CMPs. Attenuated total reflectance-Fourier transform infrared spectroscopy (ATR−FTIR) was used to characterize the synthesized CMPs and confirm the cross-coupling between aryl halide and terminal alkyne during the polymer synthesis. As shown in Figure 1A, a strong peak at 3286 cm^{-1} (−C≡C−H stretch in terminal alkyne) was observed in the monomer, 1,3,5-triethynylbenzene (red), but was almost diminished in both the CMP-1 (black) and CMP-2 (blue) samples. At the same time, a new peak at 2200 cm^{-1} that was ascribed to R−C≡C−R′ appeared in both CMP-1 and CMP-2.[36] Taken together, the decrease at 3286 cm^{-1} and increase at 2200 cm^{-1} suggest the highly efficient cross-coupling between aryl halide and terminal alkyne during the synthesis of CMP-1 and CMP-2. The FTIR spectra were also collected to compare the structural changes among the CMPs and the carbonized CMPs (Figure 1B). Briefly, the peak at 3286 cm^{-1} (−C≡C−H) was diminished in all carbonized CMPs, suggesting that the cross-coupling proceeded to a greater extent after carbonization. The main peaks observed at 1440 and 1100 cm^{-1} correspond to the aromatic skeletons and substituted aromatic hydrocarbons, respectively. Similar peaks in the fingerprint region (from 1500 to 500 cm^{-1}) were also observed for all of the carbonized CMPs.[37] The observed trends validate the formation of conjugated clusters during the pyrolysis. The complete list of peak assignments is provided in Table S1 of the Supporting Information.

To further characterize the structures of CMPs and carbonized CMPs at the molecular level, solid-state ^{13}C multi-CP/MAS NMR was used to confirm the assignment of the resonances, and the list of peak assignments is provided in Table S2 of the Supporting Information. As shown in Figure 2A, the peaks at 123.7 ppm ($C_{Ar}-C\equiv C-C_{Ar}$), 131.8 ppm (C_{Ar-H}), and 90.8 ppm ($C_{R-C\equiv C-R'}$) suggest the formation of conjugated polymer networks in both CMP-1 and CMP-2. Moreover, the peaks at 167.8 ppm (C_{Ar-OH}) and 196.2 ppm ($C_{Ar=O}$) for CMP-2 indicate the successful incorporation of the phenolic and carbonyl groups, respectively, in the polymer network. To probe the degree of polymerization, peak-differentiation-imitating NMR analysis was used.[38,39] Specifically, the peak at 90.8 ppm ($C_{R-C\equiv C-R'}$) suggests the efficient coupling between the aryl halides and alkynes.[26,32] Moreover, the ratio of the low-intensity peak at 80.3 ppm ($C_{-C\equiv C-H}$) over the peak at 90.8 ppm ($C_{R-C\equiv C-R'}$) provides information on the degree of condensation, where a smaller value corresponds to a higher degree of polymerization. The ratios calculated from our results were 0.18 and 0.15 for CMP-1 and CMP-2, respectively, suggesting a high degree of condensation. Our results were consistent with previously reported values.[32,40]

The structures of the carbonized CMPs from the slow pyrolysis of CMP-1 were distinctively different from CMP-1 and CMP-2 (Figure 2B). In particular, the peak at 90.8 ppm ($C_{R-C\equiv C-R'}$) disappeared, and a new peak for aromatic carbon (100−165 ppm) was detected for all of the carbonized CMPs. The NMR spectra of the carbonized CMPs were then fitted with three Gaussian peaks to obtain information on the protonated aromatic carbon at 108.5 ppm, the non-protonated aromatic carbon at 129.6 ppm, and the aromatic branched carbon at 142.2 ppm (Table S3 and Figure S1 of the Supporting Information).[41] The obtained information was used to calculate the aromatic cluster size (θ_b) of the carbonized CMPs using eqs 4−6

$$\theta_b = \frac{f_a^B}{f_a} \tag{4}$$

$$f_a = \frac{A_{100-165\ \mathrm{ppm}}}{A_{0-220\ \mathrm{ppm}}} \quad (5)$$

$$f_a^B = \frac{A_{129\ \mathrm{ppm}}}{A_{0-220\ \mathrm{ppm}}} \quad (6)$$

where θ_b is the aromatic cluster size of the CMPs, f_a^B is the fraction of bridgehead carbon in the total carbon, f_a is the fraction of aromatic carbon in the total carbon, $A_{100-165\ \mathrm{ppm}}$ is the integrated spectral intensity in the aromatic region, and $A_{0-220\ \mathrm{ppm}}$ is the integrated intensity of the entire spectrum.

As shown in Table 1, the average cluster size of the carbonized CMPs increased as the pyrolysis temperature increased from 600 to 900 °C, suggesting that more graphitic regions were formed at higher temperatures. This was further supported by our conductivity measurement results (Figure S2 of the Supporting Information). Specifically, the conductivity of the carbonized CMPs increased by 6 orders of magnitude (from 60.9 μS/m to 63.68 S/m) as the pyrolysis temperature increased from 600 to 900 °C. In contrast, both CMP-1 and CMP-2 were barely conductive (below 28.5 μS/m). All of the CMPs and carbonized CMPs exhibited high surface area, microporosity, and mesoporosity (Figure S3 of the Supporting Information). As the pyrolysis temperature increased from 600 to 900 °C, the surface area of the carbonized CMPs first increased to a maximum of 1133 m^2/g at 700 °C and then decreased. We propose that the initial increase in the surface area was likely due to the generation of pores and cracking in the matrix of CMPs.[42] As the pyrolysis temperature further increased to 900 °C, the porosity partially collapsed and, thus, resulted in the decrease of the surface area.

Table 1. Chemical and Physical Properties of CMPs

	cluster size, θ_b	conductivity, σ (S/m)	surface area (m^2/g)	EDC (mmol$_{e-}$/g)
CMP-1	N.D.[a]	1.96×10^{-7}	398.8	N.D.
CMP-2	N.D.	2.85×10^{-7}	133.3	1.859 ± 0.073
CMP-1-600	0.635	6.09×10^{-7}	617.7	0.296 ± 0.036
CMP-1-700	0.668	0.187	1132.8	1.831 ± 0.137
CMP-1-800	0.704	24.42	975.5	2.186 ± 0.092
CMP-1-900	0.828	63.68	659.0	2.003 ± 0.127

[a] N.D.: not determined.

Transformation of TCNM in the Presence of the CMPs. TCNM was chosen as a model pollutant to quantify the reactivity of the synthesized polymers (CMP-1, CMP-2, and carbonized CMPs). The degradation of TCNM was first monitored in the batch reactors in the presence of 0.7 g/L CMP-1-800 at pH 7. The total mass of TCNM was retrieved from both the aqueous and solid phases as previously described. The extraction efficiencies of TCNM from CMP-1, CMP-2, and carbonized CMPs were provided in Table S4 of the Supporting Information. Over 86% of TCNM disappeared within the first 5 min in the presence of CMP-1-800 alone (Figure 3A). In contrast, no decay of TCNM was observed in the controls containing only buffer (Figure S4 of the Supporting Information). As TCNM disappeared, the formation of DCNM was observed as the major organic product and the concentration of DCNM increased to a maximum of 0.065 μmol in 15 min. A small amount of CNM was also observed, suggesting the further dechlorination of DCNM. Moreover, chloride was formed as TCNM disappeared. The molar ratio of TCNM decay over the formation of chloride was 1:1.27 after 20 min. The overall mass recovery of chlorine was 80% after 20 min. Taken together, our results suggest that CMP-1-800 is intrinsically reactive and can facilitate the abiotic transformation of TCNM at pH 7. The degradation of TCNM possibly involves a stepwise dechlorination pathway based on the characterized transformation products, including DCNM, CNM, and chloride.

The reactivity of the other CMPs and the carbonized CMPs with TCNM was also investigated (Figure 3B). The decay of TCNM was only observed in the presence of the carbonized CMPs (CMP-1-700, CMP-1-800, and CMP-1-900) that were produced at pyrolysis temperatures of 700 °C or above. The observed TCNM decay followed pseudo-first-order kinetics in the presence of the carbonized CMPs (Figure S5 of the Supporting Information). As presented in Figure 3B, CMP-1-800 exhibited the highest reactivity (k_{obs} = 0.29 ± 0.047 min^{-1}), followed by CMP-1-900 (k_{obs} = 0.195 ± 0.014 min^{-1}) and CMP-1-700 (k_{obs} = 0.092 ± 0.008 min^{-1}). A model PCM,

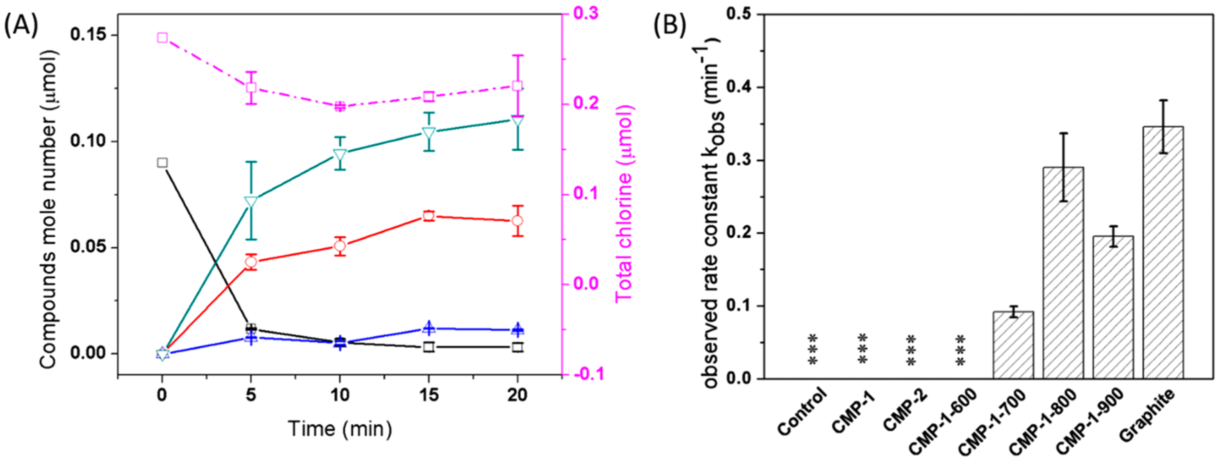

Figure 3. (A) TCNM degradation and product formation in the presence of 0.7 g/L CMP-1-800 at pH 7: mass balance on the total chlorine (pink); TCNM (black); CNM (red); and chloride (green). (B) Rate constants for TCNM decay in the presence of 0.7 g/L CMPs at pH 7, where *** indicates that the decay of TCNM was negligible during the experimental time frame. Controls are samples containing buffer in the absence of CMPs at pH 7. The error bars represent the standard deviations of the experimental duplicate.

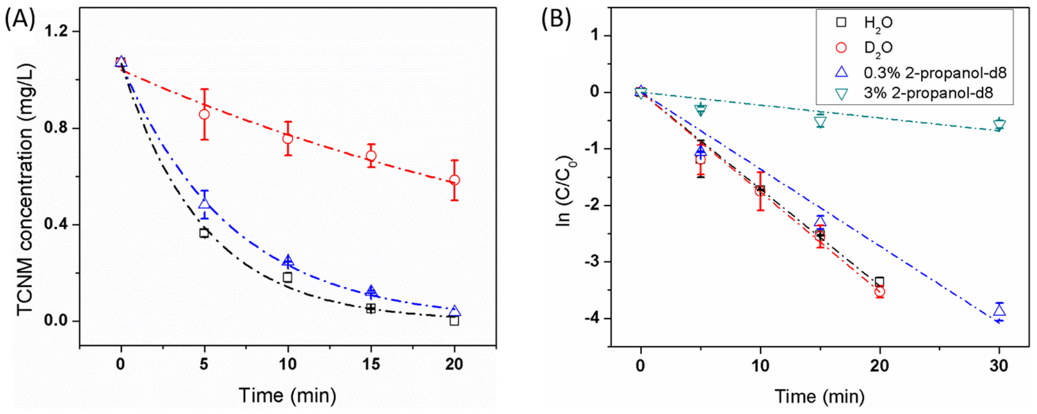

Figure 4. (A) Decay of TCNM at 25 °C in the presence of CMP-1-900 in 10 mM phosphate buffer at pH 7 (black), carbonate buffer at pH 8 (red), and carbonate buffer at pH 10 (blue). (B) Pseudo-first-order decay for TCNM in the presence of 5 g/L CMP-1-900 at pH 7. Both H_2O and D_2O were used as the solvent. 2-Propanol-d_8 was also added at 0.3 and 3% by volume to trap the formed radicals. The error bars represent the standard deviations of the experimental duplicate.

namely, graphite powder, demonstrated similar reactivity in promoting TCNM decay when compared to CMP-1-800 (k_{obs} = 0.346 ± 0.036 versus 0.29 ± 0.047 min^{-1}). Our results suggest that the synthesized CMPs may show similar reactivity in pollutant removal compared to PCM. Details of TCNM decay and the formation of its products in the presence of graphite were provided in Figure S9 of the Supporting Information. In contrast, no reactivity toward TCNM was observed for CMP-1, CMP-2, or CMP-1-600. Furthermore, the controls containing 0.14 g/L palladium(0), the catalyst used in the CMP-1 synthesis, exhibited no TCNM decay, thereby strongly suggesting that palladium(0) did not contribute to the observed reactivity of the CMPs (Figure S4A of the Supporting Information). Overall, the observed reaction rate roughly followed the conductivity trend of the CMPs and the carbonized CMPs, thereby indicating that the electron transfer kinetics at interfaces may play an important role in TCNM decay.

Reaction Mechanism of the TCNM Decay. On the basis of the identified transformation products of the TCNM decay, we propose that TCNM decay followed a stepwise reductive dechlorination pathway, as presented in Scheme S1 of the Supporting Information. The effect of the pH on the TCNM decay rate was first investigated to confirm the proposed reaction pathway. Specifically, the decay of TCNM was monitored in batch reactors containing CMP-1-900 over a pH range of 7−10. The results present the total mass of TCNM retrieved from both the aqueous and solid phases at various time intervals. The highest reaction rate (k_{obs} = 0.195 ± 0.014 min^{-1}) was observed at pH 7 (Figure 4A). The observed reaction rate constant decreased to 0.114 ± 0.007 min^{-1} as the pH increased to pH 8 and further decreased to 0.026 ± 0.001 min^{-1} at pH 10. These results are in line with the proposed reductive dechlorination pathway, where lower pH conditions favor the reaction and CMPs act as the reductants by donating electrons to TCNM. Accordingly, we postulate that the reductive dechlorination of TCNM involves two steps (Scheme S1 of the Supporting Information): (1) the dissociative electron transfer to a C−Cl bond with the formation of an organochloride radical and the release of chloride and (2) the transfer of a second electron and protonation.[43,44] To discern the rate-limiting step, we carried out trapping experiments using both D_2O and 2-propanol-d_8. 2-Propanol-d_8 is known to be a better D donor than D_2O.[45] As shown in Figure 4B, no significant differences in TCNM decay rates were observed in reaction systems containing CMP-1-900 in the presence of H_2O versus D_2O. However, when 2-propanol-d_8 was introduced to reaction systems containing CMP-1-900 and H_2O, the decay rate of TCNM quickly decreased. As the volume of 2-propanol-d_8 increased from 0 to 0.3 to 3%, the decay rates of TCNM decreased from 0.171 ± 0.006 to 0.136 ± 0.006 to 0.023 ± 0.005 min^{-1}. Moreover, both DCNM and d-DCNM were observed during the TCNM transformation by CMP-1-900 in the presence of D_2O after 20 min. In contrast, the formation of d-DCNM was almost negligible when 2-propanol-d_8 (3% by volume) was used during the same time frame.

Taken together, our results suggest that the first step of the reaction, namely, the dissociative electron transfer from CMP-1-900 to TCNM, was the rate-limiting step. This is supported by our trapping experiment results where the decay rates of TCNM were decreased when 2-propanol-d_8 was added to the system. We propose that 2-propanol-d_8 was able to effectively quench the radicals formed on the surface of CMP-1-900 after the dissociative electron transfer to TCNM, which thereby led to the decrease in the transformation rate of TCNM, as shown in Scheme S1 of the Supporting Information. D_2O, on the other hand, was not able to quench the radical formed on CMP-1-900 effectively as a result of the fact that D_2O is a weaker D donor and does not have the same affinity to the solid phase compared to 2-propanol-d_8. The results of D incorporation in the formation of d-DCNM from D_2O and 2-propanol-d_8 further supported our hypothesis. Specifically, if the second step is the rate-limiting step, we would expect the reaction to slow down by replacing H_2O with D_2O. However, we did not see such an effect on the decay of TCNM. Although little d-DCNM was formed when 2-propanol-d_8 was added to the system, the reaction rate for TCNM decay was significantly decreased. Taken together, our results demonstrate that the dissociative electron transfer from CMP-1-900 to TCNM rather than the transfer of a second electron and protonation was the rate-limiting step for the observed TCNM transformation.

Mass Transfer of TCNM from Solution to CMPs. To understand the surface reaction between TCNM and CMPs, the mass transfer of TCNM from solution to the solid phase of

DOI: 10.1021/acs.est.9b01772
Environ. Sci. Technol. 2019, 53, 7673−7682

CMPs was first analyzed. Adsorption kinetic experiments were carried out in methanol to eliminate surface reactions. The homogeneous surface diffusion model (HSDM) was used to fit our kinetic data using the method described in previous publications.[46−48] Details were provided in Text S2 of the Supporting Information. Briefly, we carried out the adsorption isotherm and kinetic experiments of TCNM in the presence of CMP-1-700, CMP-1-800, and CMP-1-900, respectively. The adsorption kinetic data were then used to obtain the surface diffusion coefficient (D_s) for TCNM on CMPs, which were 4.21×10^{-11} cm^2 s^{-1} for CMP-1-700, 1.33×10^{-11} cm^2 s^{-1} for CMP-1-800, and 0.682×10^{-11} cm^2 s^{-1} for CMP-1-900, respectively.

The Langmuir kinetic model was also used to fit our adsorption kinetic data for comparison purposes following the method described in our previous publications.[10,49] Briefly, the mass transfer of TCNM from solution to the solid phase can be described by eqs 7 and 8, where q is the solid-phase concentration of TCNM (mg/g), k_a is the rate constant (L mg^{-1} h^{-1}) associated with the solution-to-solid mass transfer (i.e., sorption) of TCNM, C is the aqueous concentration (mg L^{-1}), Q is the total number of sorption sites (mg g^{-1}), and k_d is the rate constant (h^{-1}) associated with the solid-to-solution mass transfer (i.e., desorption) of TCNM. The adsorption capacities (Q) of CMP-1-700, CMP-1-800, and CMP-1-900 were determined experimentally by increasing the TCNM concentrations in methanol. Q was subsequently determined on the basis of the plateau regions of the curves (Figure S6A of the Supporting Information), which were 2.59, 2.3, and 0.7 mg/g for CMP-1-700, CMP-1-800, and CMP-1-900, respectively. Experiments on the sorption kinetics of TCNM were then carried out with each of the three CMPs (0.7 g/L) in methanol, where an excess of TCNM (10 mg/L) was present. As a result, the aqueous-phase concentration of TCNM (C) can be treated as a constant in eq 7 because it only decreased less than 10% during the experimental time frame. Accordingly, both k_a and k_d were obtained by exponential regression using eq 7 (Figure S6B of the Supporting Information).

$$\frac{dq}{dt} = k_a C Q - (k_a C + k_d) q \tag{7}$$

$$\frac{dC}{dt} = k_d q - k_a C(Q - q) \tag{8}$$

Subsequently, both the HSDM and Langmuir kinetic model with optimized parameters were used to validate the adsorption kinetic data. Results were shown in Figure S7 of the Supporting Information. To compare the goodness-of-fit of the model to measured data, coefficient of determination (COD) values were calculated using eq 9 for both models:

$$\text{COD} = \frac{\sum_{j=1}^{5} (\overline{C}_1^{\text{model}} - \overline{\overline{C}^{\text{data}}})^2}{\sum_{j=1}^{5} (\overline{C}_j^{\text{model}} - \overline{\overline{C}^{\text{data}}})^2 + \sum_{j=1}^{5} (\overline{C}_j^{\text{model}} - \overline{C}_j^{\text{data}})^2} \tag{9}$$

Results were summarized in Table S7 of the Supporting Information. The much higher COD values for the Langmuir kinetic model suggest that it is better suited for our experimental condition. Therefore, we proceeded with the Langmuir kinetic model to determine the surface reaction of TCNM and CMPs in the following section.

Surface Reaction Rates of the TCNM Decay. As shown in eq 10, the decay of TCNM in the batch reactors containing CMPs was the sum of several competing processes based on the Langmuir kinetic model:[10,49] (1) the adsorption (k_a) of TCNM from the aqueous phase to the surface of CMPs, (2) the desorption (k_d) of TCNM from the surface of CMPs back to the aqueous solution, and (3) the surface reaction (k_{rxn}) between adsorbed TCNM and CMPs

$$\frac{dq}{dt} = k_a C(Q - q) - k_d q - k_{rxn} q \tag{10}$$

where $Q - q$ represents the concentration of the vacant sorption sites, k_{rxn} is the surface rate constant (h^{-1}), and all other parameters were defined in the previous section.

To obtain the reaction rate constant (k_{rxn}) of the surface reaction between TCNM and CMPs, the TCNM decay was monitored in the presence of the CMPs at pH 7 in H_2O to allow for the surface reactions. Previously obtained k_a and k_d were substituted into eq 10, and the remaining parameters, C and q, were determined experimentally at each time point. Data were fitted using both eqs 8 and 10. MATLAB was used to solve for k_{rxn}. The concentrations of TCNM in the aqueous and solid phases at time zero were applied as initial conditions: $C(0) = 1.11$ mg/L and $q(0) = 0$. The time progression (t) was set at a fixed step size of 0.001 h. The obtained k_{rxn} values are summarized in Table 2, where CMP-1-900 showed the highest reactivity ($k_{rxn} = 7.700 \pm 1.674$ min^{-1}), followed by CMP-1-800 ($k_{rxn} = 5.087 \pm 0.989$ min^{-1}) and CMP-1-700 ($k_{rxn} = 1.579 \pm 0.077$ min^{-1}). The model fitting curves are provided in Figure S7 of the Supporting Information with calculated COD values of 0.95, 0.84, and 0.82.

Table 2. Sorption Kinetic Rate Constants and Surface Reaction Rate Constants for TCNM and CMPs at pH 7[a]

	k_a (L mg^{-1} h^{-1})	k_d (h^{-1})	k_{rxn} (min^{-1})
CMP-1-700	1.949 ± 0.349	0.785 ± 0.029	1.579 ± 0.077
CMP-1-800	4.571 ± 0.295	1.515 ± 0.042	5.087 ± 0.989
CMP-1-900	13.063 ± 0.675	6.406 ± 0.249	7.700 ± 1.674

[a] Parameters are obtained from model fitting using the Langmuir kinetic model.

Dependence of the TCNM Decay upon the CMPs Properties. To understand which properties of CMPs are responsible for their redox reactivity, correlation analyses were carried out. Specifically, the previously obtained k_{rxn} values for TCNM decay were correlated against either the conductivity or the EDC values of the CMPs. All of the EDC values were quantified using the titration method as previously described and are summarized in Table 1.[35] No strong correlation was observed between the EDC values of CMPs and the k_{rxn} of the TCNM decay (Figure 5A). Although the EDC values of CMP-2 (1.859 ± 0.073 mmol$_{e^-}$/g) and CMP-1-700 (1.831 ± 0.137 mmol$_{e^-}$/g) were comparable, their reactivities toward TCNM decay were significantly different. In particular, CMP-2 showed no reactivity, despite its high EDC value that resulted from the incorporation of phenolic moieties during the CMP-2 synthesis. In contrast, CMP-1-700 fostered the rapid decay of TCNM ($k_{rxn} = 1.579 \pm 0.077$). Overall, our results suggest that the phenolic moieties of CMPs did not result in the reduction of TCNM, despite their high EDC values, and, therefore, are not responsible for the observed redox reactivity of CMPs in this case.

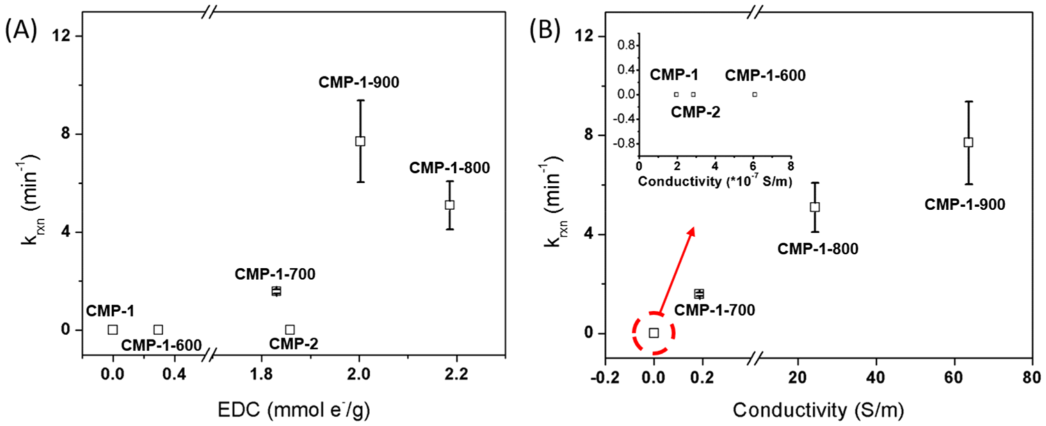

Figure 5. Correlation analyses between the model fitted rate constants (k_{rxn}) for the decay of TCNM at pH 7 against the (A) measured EDC values of CMPs and (B) conductivity of the CMPs.

Subsequently, the conductivity of the CMPs was investigated. As shown in Figure 5B, a positive correlation was observed between the conductivity of the CMPs and k_{rxn} for the decay of TCNM decay. In particular, an increase in the conductivity from 0.196 μS/m to 63.68 S/m corresponded to an increase in the decay rate of TCNM from 0 to 7.7 min^{-1} at pH 7. We propose that the observed strong correlation between the conductivity of the CMPs and the observed TCNM decay was due to the first electron transfer from CMPs to TCNM being the rate-limiting step. It is conceivable that both the pool of electrons (e.g., EAC or EDC) and the electron transfer rate at the interface can contribute to the redox reactivity of CMPs in mediating the reduction of pollutants. However, in the case of CMP-2, the first electron transfer at the interface was too slow, as reflected in its low conductivity. As a result, despite the high EDC value, the majority of the pool of electrons cannot be used for the reduction of TCNM. In addition, we propose that the observed differences in reactivity among the CMPs were likely due to a combination of factors including, for example, the electron transfer rate at the interface and the ability of the CMPs to stabilize the formed radicals on the surface. Overall, our results suggest that the conductivity of CMPs rather than the phenolic moieties or EDC played a predominant role in their redox reactivities toward the reduction of pollutants. It is important to notice that the previous study where phenolic moieties were found to be responsible for the associated EDC applied a mediated electrochemical approach, where the electron transfer kinetics at the interfaces were not rate-limiting as a result of the addition of mediators.[21] However, in our system, the electron transfer to TCNM is evidently the rate-limiting step.

■ ASSOCIATED CONTENT

Ⓢ Supporting Information

The Supporting Information is available free of charge on the ACS Publications website at DOI: 10.1021/acs.est.9b01772.

> Details of chemicals, mass transfer analysis of TCNM, peak assignments of FTIR and ^{13}C Multi-CP/MAS spectra, extraction efficiencies, surface area and pore size measurements, adsorption isotherms, details of TCNM decay kinetics, SEM images, EDC measurements, GC/MS results for *d*-DCNM and *d*-CNM, contact angle for CMP-1 and CMP-2, and proposed reaction pathway (PDF)

■ AUTHOR INFORMATION

Corresponding Author

*Telephone: 610-519-8549. Fax: 610-519-6754. E-mail: wenqing.xu@villanova.edu.

ORCID

Wenying Chu: 0000-0002-0809-5222
Wenqing Xu: 0000-0002-9838-8220

Notes

The authors declare no competing financial interest.

■ ACKNOWLEDGMENTS

Zhao Li and Wenqing Xu thank the National Science Foundation CAREER Award (CBET-1752220) for the financial support. Any opinions, findings, and conclusions or recommendations expressed in this material are those of the authors and do not those reflect the views of the National Science Foundation. Wenqing Xu thanks the National Natural Science Foundation of China (41728007) for the travel support. Zhao Li and Wenqing Xu also acknowledge Prof. John Sivey at Towson University for his inputs on the reaction mechanism discussion, Prof. Charles Coe at Villanova University for his help with the BET surface measurements, and Prof. Gang Feng at Villanova University for his assistance with the SEM images.

■ REFERENCES

(1) Roberts, K. G.; Gloy, B. A.; Joseph, S.; Scott, N. R.; Lehmann, J. Life cycle assessment of biochar systems: Estimating the energetic, economic, and climate change potential. *Environ. Sci. Technol.* **2010**, *44* (2), 827−833.

(2) Pignatello, J.; Mitch, W. A.; Xu, W. Activity and reactivity of pyrogenic carbonaceous matter toward organic compounds. *Environ. Sci. Technol.* **2017**, *51* (16), 8893−8908.

(3) Lee, J. W.; Hawkins, B.; Day, D. M.; Reicosky, D. C. Sustainability: The capacity of smokeless biomass pyrolysis for energy production, global carbon capture and sequestration. *Energy Environ. Sci.* **2010**, *3* (11), 1695−1705.

(4) Simpson, D. R. Biofilm processes in biologically active carbon water purification. *Water Res.* **2008**, *42* (12), 2839−2848.

(5) Cao, X.; Sun, S.; Sun, R. Application of biochar-based catalysts in biomass upgrading: A review. *RSC Adv.* **2017**, *7* (77), 48793−48805.

(6) Ding, K.; Xu, W. Black carbon facilitated dechlorination of DDT and its metabolites by sulfide. *Environ. Sci. Technol.* **2016**, *50* (23), 12976−12983.

(7) Pereira, R.; Pereira, M. F. R.; Alves, M.; Pereira, L. Carbon based materials as novel redox mediators for dye wastewater biodegradation. *Appl. Catal., B* **2014**, *144*, 713−720.

(8) Chen, S.; Rotaru, A.-E.; Shrestha, P. M.; Malvankar, N. S.; Liu, F.; Fan, W.; Nevin, K. P.; Lovley, D. R. Promoting interspecies electron transfer with biochar. *Sci. Rep.* **2015**, *4*, 5019.

(9) Yu, X.; Gong, W.; Liu, X.; Shi, L.; Han, X.; Bao, H. The use of carbon black to catalyze the reduction of nitrobenzenes by sulfides. *J. Hazard. Mater.* **2011**, *198*, 340−346.

(10) Xu, W.; Pignatello, J. J.; Mitch, W. A. Role of black carbon electrical conductivity in mediating hexahydro-1,3,5-trinitro-1,3,5-triazine (RDX) transformation on carbon surfaces by sulfides. *Environ. Sci. Technol.* **2013**, *47* (13), 7129−7136.

(11) Kemper, J. M.; Ammar, E.; Mitch, W. A. Abiotic degradation of hexahydro-1,3,5-trinitro-1,3,5-triazine in the presence of hydrogen sulfide and black carbon. *Environ. Sci. Technol.* **2008**, *42* (6), 2118−2123.

(12) Van Der Zee, F. P.; Bisschops, I. A.; Lettinga, G.; Field, J. A. Activated carbon as an electron acceptor and redox mediator during the anaerobic biotransformation of azo dyes. *Environ. Sci. Technol.* **2003**, *37* (2), 402−408.

(13) Xu, S.; Adhikari, D.; Huang, R.; Zhang, H.; Tang, Y.; Roden, E.; Yang, Y. Biochar-facilitated microbial reduction of hematite. *Environ. Sci. Technol.* **2016**, *50* (5), 2389−2395.

(14) Boehm, H. P. Surface oxides on carbon and their analysis: A critical assessment. *Carbon* **2002**, *40* (2), 145−149.

(15) Montes-Morán, M.; Suárez, D.; Menéndez, J.; Fuente, E. On the nature of basic sites on carbon surfaces: An overview. *Carbon* **2004**, *42* (7), 1219−1225.

(16) Hedges, J. I.; Eglinton, G.; Hatcher, P. G.; Kirchman, D. L.; Arnosti, C.; Derenne, S.; Evershed, R. P.; Kögel-Knabner, I.; de Leeuw, J. W.; Littke, R.; Michaelis, W.; Rullkötter, J. The molecularly-uncharacterized component of nonliving organic matter in natural environments. *Org. Geochem.* **2000**, *31* (10), 945−958.

(17) Masiello, C. A. New directions in black carbon organic geochemistry. *Mar. Chem.* **2004**, *92* (1−4), 201−213.

(18) Saquing, J. M.; Yu, Y.-H.; Chiu, P. C. Wood-derived black carbon (biochar) as a microbial electron donor and acceptor. *Environ. Sci. Technol. Lett.* **2016**, *3* (2), 62−66.

(19) Liu, F.; Rotaru, A.-E.; Shrestha, P. M.; Malvankar, N. S.; Nevin, K. P.; Lovley, D. R. Promoting direct interspecies electron transfer with activated carbon. *Energy Environ. Sci.* **2012**, *5* (10), 8982−8989.

(20) Prévoteau, A.; Ronsse, F.; Cid, I.; Boeckx, P.; Rabaey, K. The electron donating capacity of biochar is dramatically underestimated. *Sci. Rep.* **2016**, *6*, 32870.

(21) Klüpfel, L.; Keiluweit, M.; Kleber, M.; Sander, M. Redox properties of plant biomass-derived black carbon (biochar). *Environ. Sci. Technol.* **2014**, *48* (10), 5601−5611.

(22) Glaser, B.; Haumaier, L.; Guggenberger, G.; Zech, W. The'Terra Preta'phenomenon: A model for sustainable agriculture in the humid tropics. *Naturwissenschaften* **2001**, *88* (1), 37−41.

(23) Sun, T.; Levin, B. D. A.; Guzman, J. J. L.; Enders, A.; Muller, D. A.; Angenent, L. T.; Lehmann, J. Rapid electron transfer by the carbon matrix in natural pyrogenic carbon. *Nat. Commun.* **2017**, *8* (1), 14873.

(24) Güzel, F.; Sayğılı, H.; Sayğılı, G. A.; Koyuncu, F.; Yılmaz, C. Optimal oxidation with nitric acid of biochar derived from pyrolysis of weeds and its application in removal of hazardous dye methylene blue from aqueous solution. *J. Cleaner Prod.* **2017**, *144*, 260−265.

(25) ShamsiJazeyi, H.; Kaghazchi, T. Investigation of nitric acid treatment of activated carbon for enhanced aqueous mercury removal. *J. Ind. Eng. Chem.* **2010**, *16* (5), 852−858.

(26) Jiang, J.-X.; Su, F.; Trewin, A.; Wood, C. D.; Campbell, N. L.; Niu, H.; Dickinson, C.; Ganin, A. Y.; Rosseinsky, M. J.; Khimyak, Y. Z.; Cooper, A. I. Conjugated microporous poly(aryleneethynylene) networks. *Angew. Chem., Int. Ed.* **2007**, *46* (45), 8574−8578.

(27) Cooper, A. I. Conjugated microporous polymers. *Adv. Mater.* **2009**, *21* (12), 1291−1295.

(28) Chinchilla, R.; Nájera, C. The Sonogashira reaction: A booming methodology in synthetic organic chemistry. *Chem. Rev.* **2007**, *107* (3), 874−922.

(29) Mochidzuki, K.; Soutric, F.; Tadokoro, K.; Antal, M. J.; Tóth, M.; Zelei, B.; Várhegyi, G. Electrical and physical properties of carbonized charcoals. *Ind. Eng. Chem. Res.* **2003**, *42* (21), 5140−5151.

(30) Lee, J.-S. M.; Wu, T.-H.; Alston, B. M.; Briggs, M. E.; Hasell, T.; Hu, C.-C.; Cooper, A. I. Porosity-engineered carbons for supercapacitive energy storage using conjugated microporous polymer precursors. *J. Mater. Chem. A* **2016**, *4* (20), 7665−7673.

(31) Stöckel, E.; Wu, X.; Trewin, A.; Wood, C. D.; Clowes, R.; Campbell, N. L.; Jones, J. T.; Khimyak, Y. Z.; Adams, D. J.; Cooper, A. I. High surface area amorphous microporous poly(aryleneethynylene) networks using tetrahedral carbon-and silicon-centred monomers. *Chem. Commun.* **2009**, No. 2, 212−214.

(32) Jiang, J.-X.; Su, F.; Trewin, A.; Wood, C. D.; Niu, H.; Jones, J. T.; Khimyak, Y. Z.; Cooper, A. I. Synthetic control of the pore dimension and surface area in conjugated microporous polymer and copolymer networks. *J. Am. Chem. Soc.* **2008**, *130* (24), 7710−7720.

(33) Lowell, S.; Shields, J. E.; Thomas, M. A.; Thommes, M. *Characterization of Porous Solids and Powders: Surface Area, Pore Size and Density*; Springer Science & Business Media: Dordrecht, Netherlands, 2012; Vol. *16*, DOI: 10.1007/978-1-4020-2303-3.

(34) Johnson, R. L.; Schmidt-Rohr, K. Quantitative solid-state ^{13}C NMR with signal enhancement by multiple cross polarization. *J. Magn. Reson.* **2014**, *239*, 44−49.

(35) Matsumura, Y.; Takahashi, H. Potentiometric redox titration of quinone in carbon black with $NaBH_4$ and I_2. *Carbon* **1979**, *17* (2), 109−114.

(36) Pretsch, E.; Buehlmann, P.; Affolter, C. *Structure Determination of Organic Compounds*; Springer: Berlin, Germany, 2000; DOI: 10.1007/978-3-662-04201-4.

(37) Keiluweit, M.; Nico, P. S.; Johnson, M. G.; Kleber, M. Dynamic molecular structure of plant biomass-derived black carbon (biochar). *Environ. Sci. Technol.* **2010**, *44* (4), 1247−1253.

(38) Tang, X.-P.; Kleinhammes, A.; Shimoda, H.; Fleming, L.; Bennoune, K.; Sinha, S.; Bower, C.; Zhou, O.; Wu, Y. Electronic structures of single-walled carbon nanotubes determined by NMR. *Science* **2000**, *288* (5465), 492−494.

(39) Mao, J.-D.; Schmidt-Rohr, K. Recoupled long-range C-H dipolar dephasing in solid-state NMR, and its use for spectral selection of fused aromatic rings. *J. Magn. Reson.* **2003**, *162* (1), 217−227.

(40) Dawson, R.; Laybourn, A.; Clowes, R.; Khimyak, Y. Z.; Adams, D. J.; Cooper, A. I. Functionalized conjugated microporous polymers. *Macromolecules* **2009**, *42* (22), 8809−8816.

(41) Dawson, R.; Laybourn, A.; Khimyak, Y. Z.; Adams, D. J.; Cooper, A. I. High surface area conjugated microporous polymers: The importance of reaction solvent choice. *Macromolecules* **2010**, *43* (20), 8524−8530.

(42) Downie, A.; Crosky, A.; Munroe, P. Physical properties of biochar. In *Biochar for Environmental Management: Science and Technology*; Lehmann, J., Joseph, S., Eds.; Earthscan: London, U.K., 2009; pp 13−32.

(43) Pecher, K.; Haderlein, S. B.; Schwarzenbach, R. P. Reduction of polyhalogenated methanes by surface-bound Fe(II) in aqueous suspensions of iron oxides. *Environ. Sci. Technol.* **2002**, *36* (8), 1734−1741.

(44) Elsner, M.; Haderlein, S. B.; Kellerhals, T.; Luzi, S.; Zwank, L.; Angst, W.; Schwarzenbach, R. P. Mechanisms and products of surface-mediated reductive dehalogenation of carbon tetrachloride by Fe(II) on goethite. *Environ. Sci. Technol.* **2004**, *38* (7), 2058−2066.

(45) Xiang, Y.; Li, X.; Lu, C.; Ma, L.; Zhang, Q. Water-improved heterogeneous transfer hydrogenation using methanol as hydrogen donor over Pd-based catalyst. *Appl. Catal., A* **2010**, *375* (2), 289−294.

(46) Zhang, Q.; Crittenden, J.; Hristovski, K.; Hand, D.; Westerhoff, P. User-oriented batch reactor solutions to the homogeneous surface

diffusion model for different activated carbon dosages. *Water Res.* **2009**, *43* (7), 1859−1866.

(47) Hand, D. W.; Crittenden, J. C.; Thacker, W. E. User-oriented batch reactor solutions to the homogeneous surface diffusion model. *J. Environ. Eng.* **1983**, *109* (1), 82−101.

(48) Crittenden, J. C.; Trussell, R. R.; Hand, D. W.; Howe, K. J.; Tchobanoglous, G. *MWH's Water Treatment: Principles and Design*; John Wiley & Sons: Hoboken, NJ, 2012; DOI: 10.1002/9781118131473.

(49) Ding, K.; Byrnes, C.; Bridge, J.; Grannas, A.; Xu, W. Surface-promoted hydrolysis of 2,4,6-trinitrotoluene and 2,4-dinitroanisole on pyrogenic carbonaceous matter. *Chemosphere* **2018**, *197*, 603−610.